Paper V

Acoustic Loss Mechanisms in Leaky SAW Resonators on Lithium Tantalate

Julius Koskela, Jouni V. Knuuttila, Tapani Makkonen, *Member, IEEE*,
Victor P. Plessky, *Member, IEEE*, and Martti M. Salomaa, *Member, IEEE*

Abstract—We discuss acoustic losses in synchronous leaky surface acoustic wave (LSAW) resonators on rotated Y-cut lithium tantalate (LiTaO$_3$) substrates. Laser probe measurements and theoretical models are employed to identify and characterize the radiation of leaky waves into the busbars of the resonator and the excitation of bulk acoustic waves. Escaping LSAWs lead to a significant increase in the conductance, typically occurring in the vicinity of the resonance and in the stopband, but they do not explain the experimentally observed deterioration of the electrical response at the antiresonance. At frequencies above the stopband, the generation of fast shear bulk acoustic waves is the dominant loss mechanism.

I. INTRODUCTION

L SAW DEVICES operating at radio frequencies are widely employed in modern telecommunication systems. In particular, LSAW resonators on rotated Y-cut LiTaO$_3$ and lithium niobate (LiNbO$_3$) substrates constitute building blocks for resonator filters, such as impedance element filters (IEFs). In the IEFs, the resonator performance at frequencies close to the resonance and the antiresonance determines the insertion loss of the device. Consequently, identifying the leakage mechanisms and minimizing the resonator losses is of major technological and commercial interest. In this paper, we consider losses in LSAW resonators on LiTaO$_3$ substrates.

LSAW on 36°-42°YX-LiTaO$_3$ contain a small slow shear bulk acoustic wave (ss-BAW) component that results in an attenuation of the LSAW. Significant reduction in this propagation loss was achieved with the discovery [1] that the coupling to ss-BAWs may be diminished by an optimal combination of the crystal cut angle and the thickness of the aluminum electrodes. However, a remaining problem is that LSAW resonators feature strong frequency-dependent losses, which lead to reduction in the filter performance
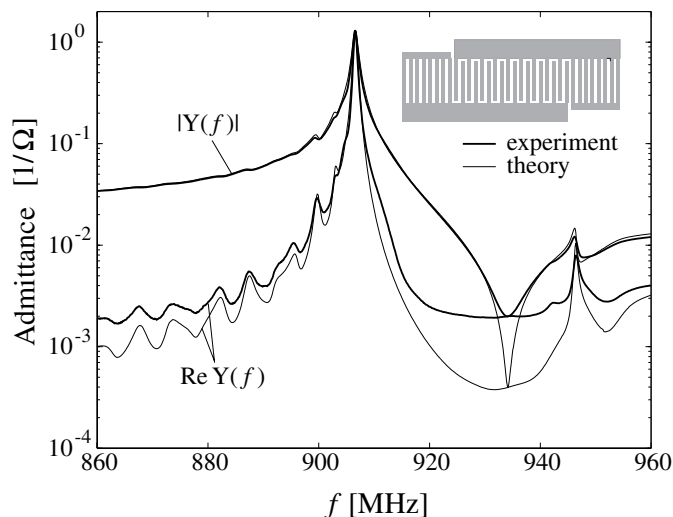

Fig. 1. Admittance and conductance of a synchronous test resonator on 36°YX-cut LiTaO$_3$ vs. a one-dimensional resonator model [8]. Despite including a series resistance as high as 0.5 Ω, the modeled conductance, *i.e.*, the losses, are too low.

and require corrections in the device design [2]. Although the role of phenomena such as backscattering into fast shear bulk acoustic waves (fs-BAW) and the synchronous excitation of fs-BAWs have been studied [3], the mechanisms underlying the losses are, for the moment, not well understood.

Our recent measurements [4] with a scanning optical Michelson laser interferometer [5] have revealed qualitatively that strong radiation of LSAWs from the active resonator region to the busbars of the device may occur at stopband frequencies [6]. Preliminary results of this work were reported in [7]. In this paper, we characterize the frequency dependence and the magnitude of the losses caused by the busbar radiation, LSAW coupling to the ss-BAW, and the generation of fs-BAWs.

The laser interferometric measurements of a test resonator are discussed in Section II, and the loss mechanisms are analyzed in Section III. A phenomenological structure model is constructed in Section IV, and the results are presented in Section V. Section VI concludes the paper.

II. LASER INTERFEROMETRIC MEASUREMENTS

Fig. 1 shows the admittance of a synchronous resonator on 36°YX-cut LiTaO$_3$ substrate. The test device has N_p

= 120 electrode pairs in the interdigital transducer (IDT) and N_g = 50 electrodes in each reflector. The pitch is p = 2.214 μm, the aperture is W = 70 μm, the relative aluminum electrode thickness is h/λ_0 = 5.6%, and the metallization ratio is about 0.5. Also shown is a fit to a one-dimensional phenomenological resonator model [8], which takes into consideration the interactions between LSAWs and fs-BAWs. The results are rather typical for the model and LSAW resonators on 36°-42°YX-LiTaO$_3$.

Although the resonance and the dispersion characteristics are satisfactorily reproduced by the model, systematic discrepancies in the conductance, representing losses, may be observed on the high frequency side of the resonance peak and in the middle of the stopband. As the most notable consequence, the predicted Q value of the antiresonance is too high. Yet, the agreement shown in Fig. 1 requires the inclusion of a parasitic series resistance of about 0.5 Ω; a reasonable theoretical estimate would be about one order of magnitude lower. Minor differences between the model and the experiments may be explained by the numerous approximations underlying our model, but the magnitude of the disagreement rather suggests the existence of additional loss mechanisms.

To study directly the acoustic activity in LSAW devices, we utilize a scanning optical Michelson interferometer [5], which detects the shear vertical component of the mechanical displacement field. Fig. 2 displays the light reflection data and a wide amplitude scan of the test resonator at the frequency f = 910 MHz, coinciding with the unpredicted lump in the conductance slightly above the resonance peak. The resonator is aligned with the crystal X-axis.

In the longitudinal device direction, the acoustic field remains confined into the active device region, as expected on the basis of one-dimensional models. However, the waves are capable of escaping from the device to the busbars. At least three separate loss mechanisms may be identified: the radiation of LSAWs to the busbars [6], synchronous waveguide radiation of Rayleigh waves [9] at an angle of about 40°, and transverse excitation of Rayleigh waves. Note that because Rayleigh waves have strong shear vertical polarization and LSAWs are essentially shear horizontal surface waves, the probe images are likely to strongly pronounce the former over the latter. Furthermore, it should be kept in mind that mechanisms such as ss-BAW radiation into the bulk and resistive and viscous losses are not revealed from surface scans.

The observed asymmetry of the probed acoustic field may be explained by the crystalline anisotropy—an inherent materials property—of the LiTaO$_3$ substrate. The LSAW velocity is a symmetric function of the propagation angle θ about the crystal X axis, see Fig. 2(a). However, the LSAW polarization is an asymmetric function of θ, and the asymmetry is particularly strong in the shear vertical component detected by the probe [6].

The series of probe images in Fig. 3 illustrates the dependence of the LSAW busbar radiation on frequency. Below the resonance frequency, the phenomenon exists
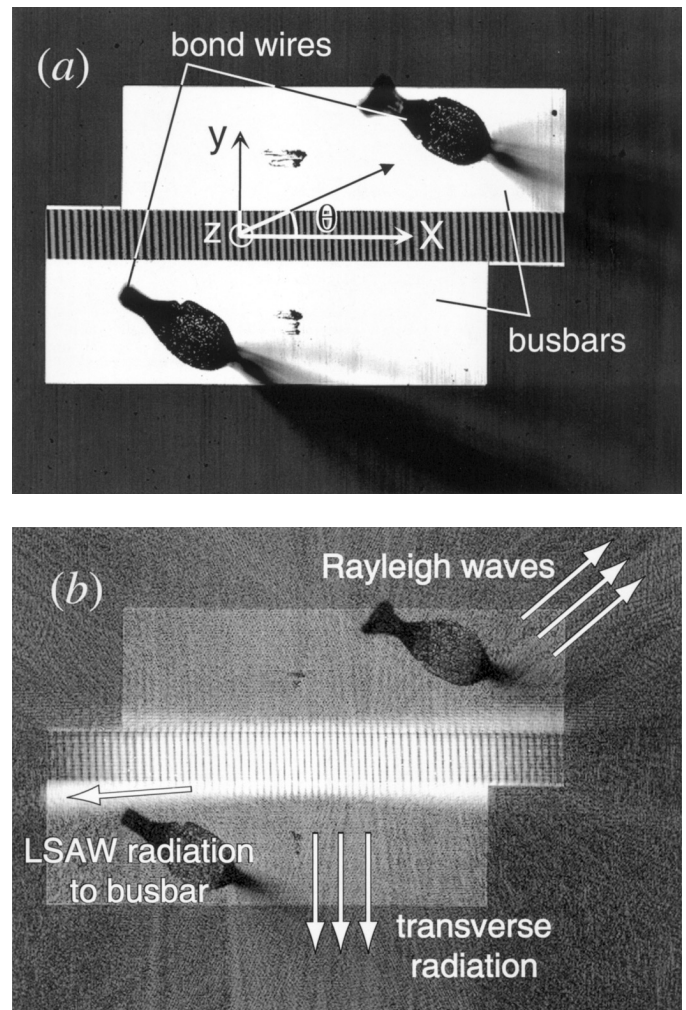
Fig. 2. Areal scan of the test resonator. a) Light reflection data; b) the shear vertical displacement field at 910 MHz, indicating three two-dimensional leakage mechanisms. The displacement is not to scale in the areas with different light reflection coefficients.

weakly; at frequencies slightly above the resonance, it is very pronounced. Close to a quenching frequency of about 918 MHz, the radiation becomes strongly suppressed and practically disappears. Similar frequency dependence may be recognized in the losses in Fig. 1, and it may be understood on the basis of the curvature of loaded slowness curves, as will be discussed subsequently.

Because of the quenching of the LSAW busbar radiation, the phenomenon is not likely to be responsible for the residual losses in the middle of the stopband. Fig. 4 shows the probed field in the resonator at the antiresonance. In the image, the radiation of obliquely propagating and transverse Rayleigh waves appear to be the most prominent acoustic loss mechanisms.

Fig. 3. Areal scans of the test resonator, featuring the frequency dependence of the LSAW radiation to the busbars. Below the resonance, the radiation is weak (a, b). Strong, spatially asymmetric radiation occurs slightly above the reso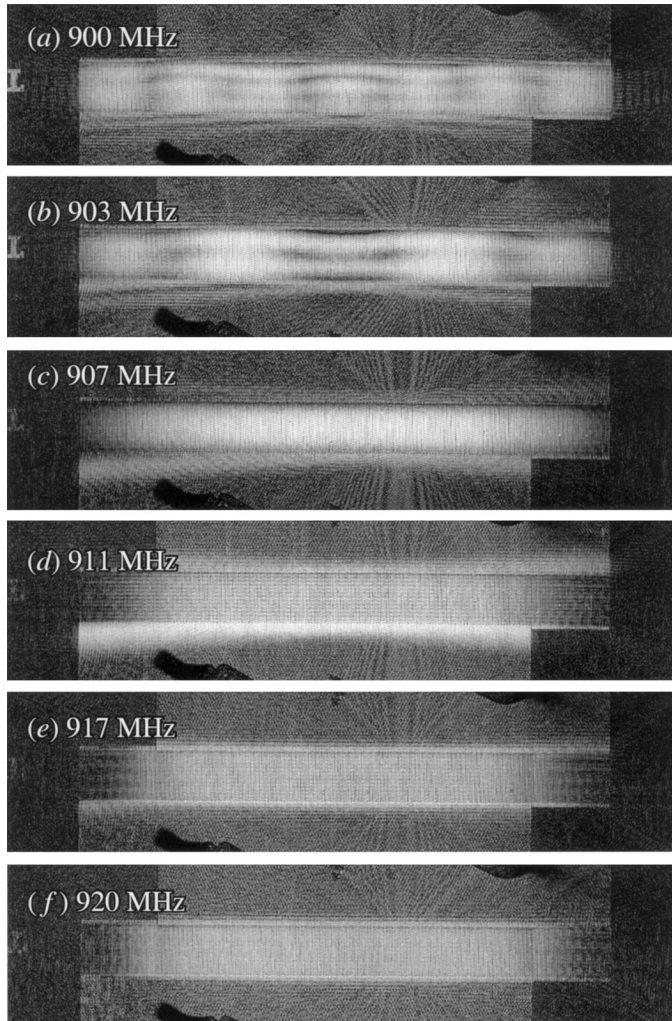nance (c, d). Toward a quenching frequency of about 918 MHz, the radiation decreases (e) and virtually disappears (f). Also scattering from a point-like imperfection in the metallization, not related to the busbar radiation, is distinguishable.
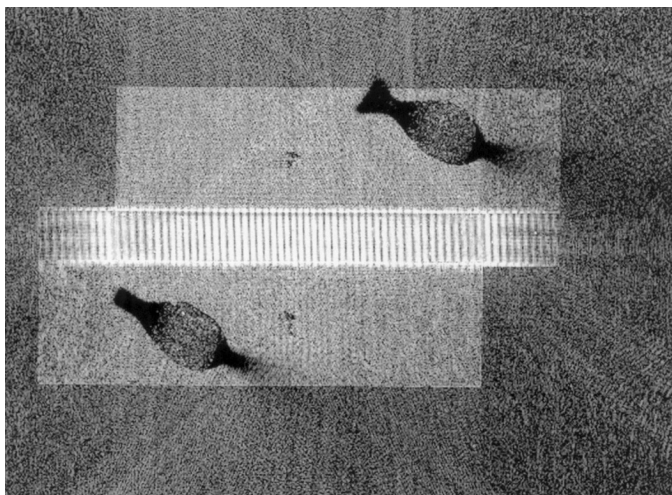

Fig. 4. Areal scan of the test resonator at 934 MHz, close to the antiresonance frequency.

III. THEORETICAL ANALYSIS

Green's function techniques were employed to analyze surface acoustic waves (SAWs), LSAWs,[1] and bulk acoustic waves (BAWs) on uniformly metallized 36°- and 42°YX-cut LiTaO$_3$ surfaces. With the exception of LSAW attenuation, the two cuts are almost identical; the results presented here are for the 42°-cut. The material parameters for the substrate were taken from [10]; aluminum was assumed isotropic, with a density of 2600 kg/m^3 and the Lamé coefficients $\mu = 2.5 \cdot 10^{10}$ N/m^2 and $\lambda = 6.1 \cdot 10^{10}$ N/m^2.

A. Leaky Waves on Metallized Crystal Surface

The LSAW slowness under an ideally conducting, uniform metal layer depends on the propagation direction θ and the product of the frequency f and the film thickness h. The slowness curves and the attenuation for various frequency-thickness products on 42°YX-cut LiTaO$_3$ are depicted in Fig. 5. The LSAW polarization is dominantly shear horizontal, and the LSAW attenuation is determined by the weak coupling to the ss-BAWs.

The slowness curves feature both convex and concave regions, implying that the direction of the energy flow varies significantly with the propagation angle. To the precision of the numerical calculations, the LSAW velocity and attenuation under a finite aluminum layer remain symmetric about the crystal X-axis—despite the asymmetry of the LSAW polarization both on free surface and under infinitely thin metallization [6].

Leaky waves attenuate because of the coupling of surface waves to ss-BAWs. For propagation along X ($\theta = 0$), the attenuation has been shown to depend strongly on the film thickness [1]. In the 36°-cut, the attenuation grows with increasing film thickness, whereas in the 42°-cut it decreases for $hf \approx 780$ m/s. However, according to our results, the attenuation increases drastically with the propagation angle for both crystal cuts and for all film thicknesses, as shown for the 42°-cut in Fig. 5(b). This behavior is very different from that of Rayleigh waves, and it suggests that high order transverse waveguide modes are likely to possess heavy propagation losses.

B. Leaky Wave Radiation to Busbars

The strong frequency dependence of the LSAW radiation to the busbars may be qualitatively understood on the basis of the curvature of the LSAW slowness curves. As illustrated in Fig. 6, these may be characterized by two thresholds: the slowness for X-propagating LSAW, s_{m0}, and the maximum x-component of the slowness, s_{m1}. Both slowness thresholds are functions of the frequency-thickness product hf.

---

[1]Mathematically, LSAWs are presented here by the poles of the relevant Green's function, which has been analytically continued [11] to complex-valued slownesses.
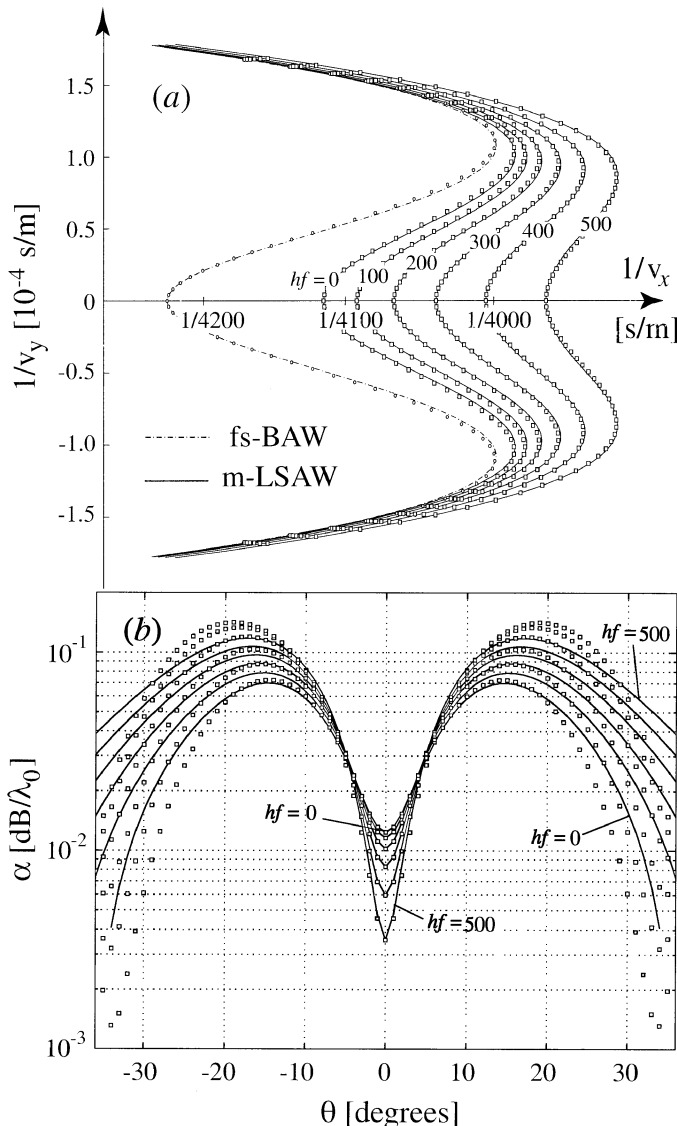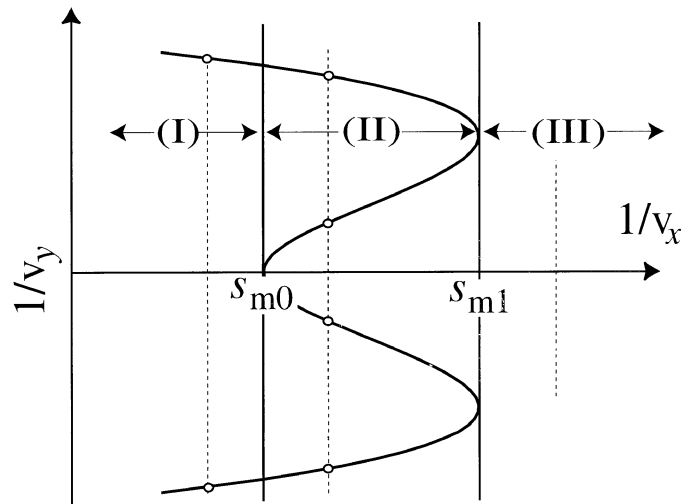
Fig. 6. Schematic LSAW slowness curve. Depending on the slowness along X, there may exist two (weak radiation regime, I), four (strong radiation regime, II), or no (radiation free regime, III) LSAW modes.

1. Weak Radiation Regime (I). For $|s_x| < s_{m0}$, the metallized surface supports a pair of LSAW eigenmodes with transverse slownesses $\pm|s_y|$. Consequently, synchronous busbar radiation is allowed, but, because the corresponding transverse wavenumbers are fairly large, the coupling to the field in the resonator is weak.

2. Strong Radiation Regime (II). For $s_{m0} < |s_x| < s_{m1}$, the metallized surface features two pairs of LSAW eigenmodes, which merge into one pair as $|s_x| \rightarrow s_{m1}$. For $|s_x| \sim s_{m0}$, the transverse slownesses are very small for one of the pairs, and acoustic energy propagates almost parallel to the crystal X-axis. Hence, the coupling to the standing wave field in the active region may be considerable, and pronounced LSAW radiation to the busbars is expected. The strength of the excitation depends on the structure.

3. Radiation Free Regime (III). For $|s_x| > s_{m1}$, there are no LSAW eigenmodes on a metallized surface. Synchronous busbar radiation is prohibited, but weak nonsynchronous radiation may occur.

This reasoning results in an important conclusion. Because the standing field slowness s_x is inversely proportional to fp and the threshold slownesses are monotonic functions of hf, corresponding frequency regimes of radiation may be determined. The relative threshold frequencies obtained only depend on the relative film thickness $h/2p$ in the busbars—they are independent of, for example, the shape and the width of the electrodes.

The results are shown in Fig. 7(b) for the 42°-cut; those for the 36°-cut are almost identical. For the metallization thickness and the pitch of the test structure, an upper threshold frequency of about 916.7 MHz is predicted. This agrees well with both the laser interferometric images and the parasitic conductance observed in Fig. 1. Indeed, the former comparison also confirms that the radiation in the weak radiation regime is very weak.

Fig. 5. a) Slowness curves and b) attenuation for LSAWs on uniformly metallized 42°YX-LiTaO$_3$ substrate for thickness-frequency products hf ranging from 0 to 500 m/s. Dotted and solid curves: rigorous calculation and the empirical model from Section IV, respectively. Dashed curves and circles: the slowness curve for fs-BAWs with their energy propagating along the crystal surface, rigorous calculation and the empirical model, respectively.

At the stopband frequencies, the standing wave field in the resonator satisfies the Bragg condition such that the wavenumbers of the dominating Fourier components along X are $k_x = \pm\pi/p$, with p denoting the mechanical periodicity. Consequently, the counterpropagating waves forming the standing field have the x slownesses

$$s_x = \pm 1/(2pf). \qquad (1)$$

Because the busbars are of uniform metal, synchronous radiation of the LSAWs into the busbars is possible if the metallized crystal surface supports propagating eigenmodes with the same x slowness [Fig. 7(a)]. Comparing the standing field slowness s_x with the threshold slownesses s_{m0} and s_{m1}, three radiation regimes are identified.
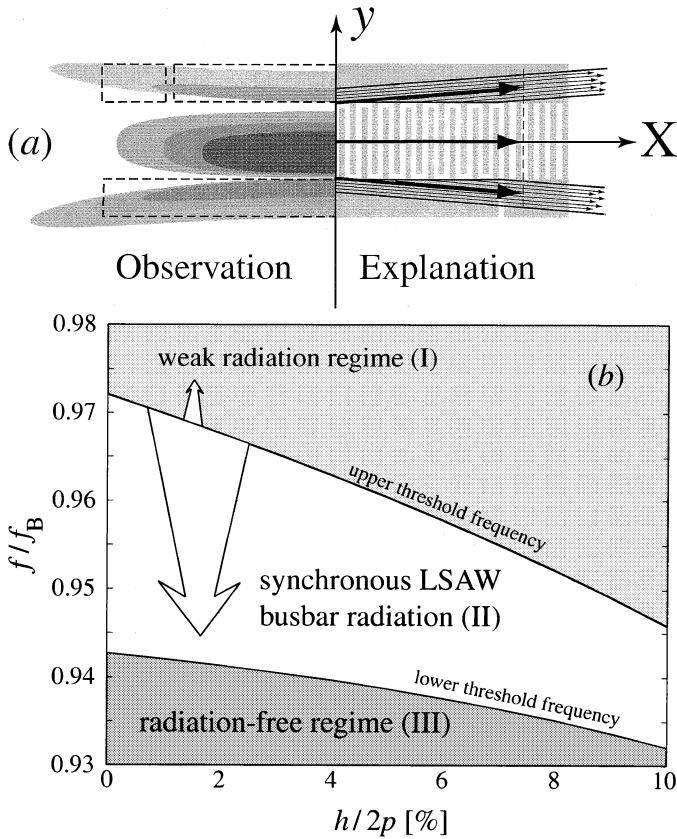
Fig. 7. a) Synchronous LSAW busbar radiation from the resonator and b) estimated relative stopband frequencies f/f_B prone to it, as a function of the relative metal thickness $h/(2p)$. Here, f_B denotes the bulk-wave threshold frequency $v_B/2p$, with $v_B = 4226.5$ m/s.

We emphasize that the analysis presented is limited to the stopband frequencies. Outside the stopband, the analysis must be based on the dispersion curve of the LSAW eigenmodes. In finite structures, small nonsynchronous LSAW radiation to the busbars may also occur. Numerical simulations of the effect of the radiation on the electrical response are presented in Section IV.

C. Rayleigh Waves and BAW

Rayleigh waves may be radiated synchronously to the busbars in the same way as LSAWs [9]. The analysis is similar to that just described, except that the Rayleigh wave velocity depends only weakly on the propagation angle and the aluminum thickness. In agreement with the laser probe results, a phase (and energy) direction with an angle of about 40° is estimated for synchronously coupled SAWs in the stopband of the test resonator.

The transverse beams seen in Fig. 2 and 4 are probably generated by the transverse electric fields in the end gaps between the busbars and the electrodes. However, increased radiation seems to originate also from the maxima of the field profile inside the resonator; this may be due to the scattering of LSAWs off the ends of the electrodes. The range of the beams vastly exceeds the surface region shown in the figures. Consequently, the beams must be surface waves. Because only Rayleigh waves are theoretically predicted to exist in this direction, the beams are identified as transversely excited Rayleigh waves.

ss-BAWs are radiated into the substrate at all frequencies of interest. The synchronous radiation of fs-BAWs occurs at high frequencies. The slowness curve for surface-skimming fs-BAWs is similar to those of LSAWs, with the threshold slownesses $s_{B0} \approx 2.366 \cdot 10^{-4}$ s/m and $s_{B1} \approx 2.501 \cdot 10^{-4}$ s/m. Consequently, off-axis synchronous fs-BAW radiation is, in principle, possible for frequencies above $0.946 f_B$, about 903 MHz in the test device. However, the much stronger on-axis synchronous fs-BAW radiation will start at 954.5 MHz in this device, as is evident in Fig. 1.

IV. PHENOMENOLOGICAL MODEL

The preceding analysis is useful for qualitative analysis of the origin and the frequency dependence of the losses, but a model is required to study the leakage mechanisms quantitatively. Because a rigorous simulation of a realistic resonator structure would require immense computational efforts, we resort to a phenomenological model with considerable computational simplification but yet covering the loss mechanisms of main interest: LSAW backscattering into fs-BAWs, busbar radiation, and synchronous fs-BAW excitation. ss-BAWs are included only through the LSAW attenuation.

Although LSAWs on LiTaO$_3$ contain weak longitudinal and shear vertical components, they are essentially shear horizontal surface waves. The shear horizontal component features almost symmetric magnitude and weak, linearly deviating phase shift as functions of the propagation angle [6]. Such behavior has been pointed to lead to a shift of the acoustic transduction amplitude with respect to the electric source [12], but here the effect is rather weak, about 0.12 wavelengths. The shear vertical displacement profiles in Fig. 2 through 4 indicate considerable transverse asymmetry, but our primitive calculations for vanishing metal thickness imply that the dominating shear horizontal field is nevertheless almost symmetric [6]. This suggests that, for rough evaluation, it suffices to consider the shear horizontal component only and to treat it as a scalar field.

Scalar waveguide theory has been used to model SAW waveguides and waveguide resonators [13]. Leaky waveguide modes have been studied in 112°-LiTaO$_3$ [14] and in ST-cut quartz [15], [16]. However, these approaches are not applicable here because of the nonconvex slowness curvature of LSAWs. For this reason, we resort to a scalar Green's function theory, empirically constructed to mimic the effects of the LSAW slowness curvature.

The grating waveguide in Fig. 8 is chosen as the model structure. It consists of an infinite periodic array of electrodes with an acoustic aperture W and two infinitely wide busbars. At the stopband frequencies, such a structure well approximates a homogeneous synchronous resonator with
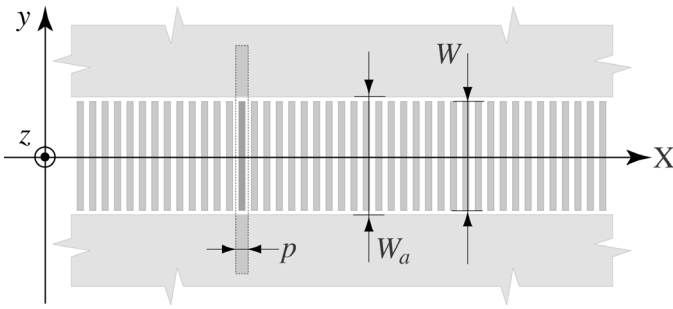
Fig. 8. Grating waveguide with infinite busbars.

long reflectors. Zhang *et al.* [17] have shown that the periodic arrays are, from the electrical point of view, completely characterized by their harmonic admittance. The concept, originally proposed for one-dimensional arrays, naturally generalizes to grating waveguides.

A. Scalar Waveguide Model

Let the wavefield be described by a scalar displacement field $u(x, y)$. Because of the existence of the device atop the surface, scalar surface stresses $T(x, y)$ may exist under the metallized surface regions. The substrate is described through a Green's function $G(x, y)$, relating the surface displacement and stress via

$$u(x, y) = \iint G(x - x', y - y')T(x', y') \; dx'dy'. \tag{2}$$

Harmonic time dependence at the angular frequency $\omega = 2\pi f$ is assumed, and it is included in the fields through an implicit factor of $e^{i\omega t}$. All fields and quantities are normalized.

The device structure is described through the boundary conditions. The source field $S(x, y)$ serves to excite waves, and electrical and mechanical perturbations of the surface are described through the load density $m(x, y)$. The net boundary condition is

$$T(x, y) = m(x, y)\omega^2 u(x, y) + S(x, y). \tag{3}$$

A model for the structure in Fig. 8 is obtained with

$$m(x, y) = m_{\rm W} + \Delta m(y) + 2m_1(y) \cos(2\pi x/p). \tag{4}$$

Here, the parameter $m_{\rm W}$ measures the loading in the infinitely wide busbars, $\Delta m(y) = m_0(y) - m_{\rm W}$, and $m_0(y)$ and $m_1(y)$ describe the uniform and periodic loading profiles in the grating, respectively.

It is practical to define the free stress field

$$\tau(x, y; m_{\rm W}) \equiv T(x, y) - m_{\rm W}\omega^2 u(x, y), \tag{5}$$

which automatically vanishes in the busbars. Consequently, it must be computed only inside the waveguide

region. Expressed through the free stress field, the constitutive relation in (2) assumes, in the Fourier domain, the form

$$\tilde{u}(k_x, k_y) = \tilde{G}(k_x, k_y; m_{\rm W})\tilde{\tau}(k_x, k_y; m_{\rm W}) \tag{6}$$

where the $m_{\rm W}$-loaded Green's function is

$$\tilde{G}(k_x, k_y; m_{\rm W}) \equiv \left[\tilde{G}^{-1}(k_x, k_y) - m_{\rm W}\omega^2 \right]^{-1}. \tag{7}$$

We emphasize that the model and, in particular, the empirical Green's function described subsequently are not proposed as tools for precise analysis, but rather as a simple method for obtaining meaningful order-of-magnitude estimates on the losses and their dependence on frequency and the device dimensions.

B. Excitation and Electric Currents

Under harmonic excitation [17], a driving voltage $V_n = V_0 e^{-i2\pi\gamma n}$ is connected to each electrode n. The currents I_n generated in the electrodes follow the phase of the voltages, such that $I_n = I_0 e^{-i2\pi\gamma n}$. Consequently, the ratio of current and voltage is the same for all electrodes; it is known as the harmonic admittance of the array.

Let $Q = 2\pi/p$ denote the grating wavenumber. To imitate the harmonic excitation in our phenomenological model, we postulate a source field of the form

$$S(x, y) = \xi_0 \sin(\pi\gamma) \left(e^{-i\gamma Q x} + e^{-i(\gamma-1)Q x} \right) \Theta(W/2 - |y|). \tag{8}$$

Here, ξ_0 is the electromechanical coupling parameter, $\Theta(x)$ denotes the Heaviside function, and W is the electric aperture. Furthermore, we assume that the acoustic contribution to the harmonic admittance is given as

$$Y_{\rm H}(\gamma, f) = i\omega 2\xi_0 \int_{-W/2}^{+W/2} u(x = 0, y) dy. \tag{9}$$

Using Fourier transformation techniques, the admittance of a synchronous resonator with N_p active electrode pairs and surrounded by two infinitely long reflectors may be expressed through the harmonic admittance as

$$Y(f) = \left[\int_0^1 Y_{\rm H}(\gamma, f) \frac{\sin^2(2\pi\gamma N_{\rm p})}{\sin^2(2\pi\gamma)} d\gamma \right] + i\omega C. \tag{10}$$

Here, the capacitance C describes the electrostatic storage of energy in the structure.

C. Empirical Green's Function

We now empirically construct an approximate Green's function that is consistent with the one-dimensional theory from [8], and that, with reasonable accuracy, produces the slowness curve for fs-BAWs and those for LSAWs under uniform metallization.

The one-dimensional Green's function from [8] is extended into two dimensions as follows:

$$\tilde{G}(k_x, k_y) = \left[\sqrt{P_{\mathrm{B}}(k_x, k_y)} - \eta(k_x, k_y) \right]^{-1}. \tag{11}$$

Here, P_{B} is a function of the form

$$P_{\mathrm{B}}(k_x, k_y) = k_x^2 + (1 + \nu)k_y^2 - k_{\mathrm{B0}}^2 \frac{1 + c\xi k_y^2/k_x^2}{1 + \xi k_y^2/k_x^2} \tag{12}$$

and η is a function of the form

$$\eta(k_x, k_y) = \frac{\eta_0 k_x^+ - \eta_1 k_{\mathrm{B0}} k_y^2/k_x^2}{1 + \eta_2 k_y^2/k_x^2}. \tag{13}$$

$k_{\mathrm{B0}} = \omega s_{\mathrm{B0}}$, where s_{B0} is the slowness for surface skimming fs-BAW, η_0 is a piezoelectric loading parameter, and k_x^+ denotes $\pm k_x$ with the sign chosen such that the real part is positive. The quantitities ν, c, ξ, η_1, and η_2 are anisotropy parameters.

The poles of the empirical Green's function represent LSAWs on a metallized crystal surface, and the branch points, i.e., the zeros of the function P_{B}, indicate the slownesses of the surface-skimming bulk waves. The slowness curves for LSAWs under uniform metallization are found from the equation

$$\tilde{G}^{-1}(k_x, k_y) = m_{\mathrm{W}} \omega^2. \tag{14}$$

Here, the loading parameter m_{W} is a monotonic function of the frequency-thickness product hf. It may be determined from rigorously computed slownesses for X-propagation $s_{x0}(hf)$ as follows

$$m_{\mathrm{W}}(hf) = \left[\sqrt{s_{x0}^2(hf) - s_{\mathrm{B0}}^2} - \eta_0 s_{x0}(hf) \right] / \omega. \tag{15}$$

In practice, finding the poles may be reduced to computing the roots of polynomials of s_y^2. The Green's function parameters were determined by fitting the slowness curves to rigorous computations for vanishing metal thickness. The resulting approximate slowness curves for the 42°-cut are compared with rigorous computations in Fig. 5, and an acceptable agreement is achieved. In addition to the modes shown in Fig. 5, the empirical Green's function may also feature unphysical poles. However, these are located deep in the complex plane, and they are of no relevance to numerical simulations.

D. Numerical Solution

The model is solved numerically using the coupling-of-modes (COM) approximation and the boundary element method (BEM). Under the harmonic excitation condition, a Floquet expansion of the displacement field yields

$$u(x, y) = \sum_{n=-\infty}^{+\infty} u_n(y) e^{-i(\gamma+n)Qx} \tag{16}$$

similarly for the stress and free stress. In the COM approximation, only the main harmonics ($n = 0$ and $n = -1$) are retained in the expansion. Introducing the same notation for the source field $S(x, y)$, the boundary conditions in the COM approximation assume the form

$$\begin{cases} \tau_0(y; m_{\mathrm{W}}) = \Delta m(y)\omega^2 u_0(y) \\ \qquad\qquad + m_1(y)\omega^2 u_{-1}(y) + S_0(y), \\ \tau_{-1}(y; m_{\mathrm{W}}) = \Delta m(y)\omega^2 u_{-1}(y) \\ \qquad\qquad + m_1(y)\omega^2 u_0(y) + S_{-1}(y). \end{cases} \tag{17}$$

The constitutive equation is

$$u_n(y) = \int_{-W/2}^{+W/2} G_{\gamma+n}(y - y'; m_{\mathrm{W}})\tau_n(y'; m_{\mathrm{W}})dy' \tag{18}$$

where

$$G_{\gamma+n}(y; m_{\mathrm{W}}) = \frac{1}{2\pi} \int \tilde{G}\left(Q(\gamma + n), k_y; m_{\mathrm{W}}\right) e^{-ik_y y}dk_y. \tag{19}$$

Substituting (18) into (17), a pair of coupled integral equations is found for the free stress field. This is solved numerically using the BEM; for the sake of brevity, the details are omitted. From the free stress field, the displacement field and the harmonic admittance are subsequently found. The electrical response of an ideal synchronous resonator is obtained as a weighted integral of the harmonic admittance.

V. ELECTRICAL RESPONSES

At the stopband frequencies, the admittance in (10) should provide a reasonable approximation to the response of a resonator with long reflectors and wide busbars. The theory was employed to model the test structure discussed in Section II.

The profiles $m_0(y)$ and $m_1(y)$ for uniform and periodic loading were assumed constants inside the electrically active waveguide region. The magnitudes m_0 and m_1 were determined to yield the correct one-dimensional dispersion relation; in the gap between the electrically active region and the busbars, the profile functions assumed one-half of these values. To describe the losses caused by ss-BAW radiation in the IDT region, additional attenuation was introduced using complex-valued frequencies; a value of $9.4 \cdot 10^{-4}$ Neper per wavelength was extracted from rigorous FEM (finite element method)/BEM simulations for a one-dimensional structure. Resistive losses in the electrodes were estimated to result in an effective series resistance of $R = 0.059\Omega$. The capacitance C was chosen to yield the correct antiresonance frequency.

The experimental and simulated admittances are compared in Fig. 9. Also shown are the scaled harmonic conductance $\mathrm{Re}Y_{\mathrm{H}}(0.5, f)$, describing a periodic IDT, and the conductance obtained for an effectively one-dimensional structure with infinite reflectors and aperture. Below the stopband frequencies, ideal (infinite) reflectors only poorly
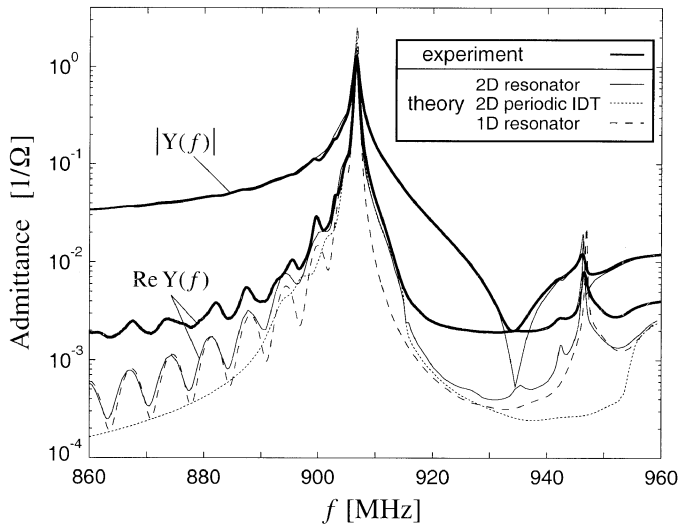
Fig. 9. Admittance and conductance of a synchronous test structure on $36°$YX-cut $LiTaO_3$ vs. a two-dimensional resonator model. For comparison, also the harmonic conductance from a two-dimensional IDT model and the conductance from a one-dimensional resonator model with infinite reflectors are shown.
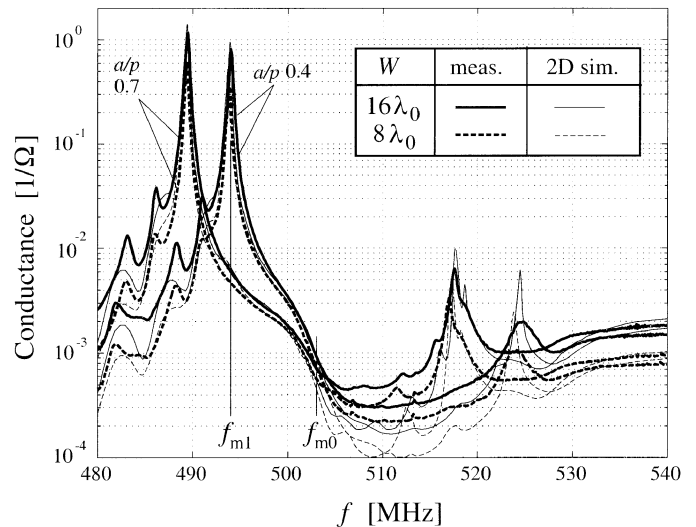

Fig. 10. Experimental and simulated conductances of four test structures with differing metallization ratios $a/p = 0.4$ and 0.7 and apertures $W = 8\lambda_0$ and $16\lambda_0$ on $42°$YX-cut lithium tantalate; also shown are the theoretically estimated frequency thresholds from Fig. 7(b).

approximate the actual finite reflectors. Consequently, the conductance oscillations occuring below the resonance are not accurately described by the model. However, close to the resonance, the losses are well reproduced.

Comparisons of the results from one- and two-dimensional models show agreement with the analysis of the LSAW busbar radiation discussed in Section III. The resulting losses are considerable, and they well explain the experimentally observed bump in the conductance. The small ripples in the experimental conductance in the stopband, appearing because of resonances of high order transverse modes, are accurately reproduced in the model.

However, the simulations provide no insight into the dominant loss mechanism close to the antiresonance. Despite the notable increase in the conductance caused by waveguide losses and the radiation of fs-BAWs, the simulated conductance values are only one-fifth of those measured experimentally. Possible causes for the unidentified losses include the excitation of ss-BAW and acoustic damping in the electrodes, made of polycrystalline aluminum. The contribution of synchronous Rayleigh-wave radiation was investigated by introducing additional poles to the scalar Green's function, but, for reasonable values of the coupling, the resulting losses were found to be almost negligible.

For frequencies close to and exceeding the threshold $f_B \approx 954.5$ MHz, the excitation of fs-BAW becomes the dominant loss mechanism.

The conductances for test structures with varying metallization ratios ($a/p = 0.3$ and 0.7) and apertures ($W = 8\lambda_0$ and $16\lambda_0$) are shown in Fig. 10. The substrate is $42°$-cut $LiTaO_3$, the pitch is $p = 4$ μm, the metal thickness is $h/\lambda_0 = 8\%$, and the resonators have 75 electrode pairs in the IDTs and 37 electrodes in each reflector. Because h and p are the same in all of the structures, the quenching of

the LSAW radiation occurs at the same frequency, about 503 MHz, in all of the structures. Another characteristic of the busbar radiation is that, in contrast to the admittance caused by LSAW propagation, it depends only weakly on the aperture. Consequently, the losses are relatively more important for narrower structures.

Finally, the S_{11} parameters of test structures with the aperture $W = 16\lambda_0$ are displayed on the Smith chart in Fig. 11 for various a/p. In this display, the region of the radiation is denoted by the thick curves. Because the stopband changes with a/p and the frequency range prone to the busbar radiation remains constant, the leakage region appears to rotate clockwise in the chart as a function of the metallization ratio.

VI. DISCUSSION

We have carried out laser interferometric measurements to study the loss mechanisms in an LSAW resonator on a $LiTaO_3$ substrate. The scanned images reveal acoustic leakage from the active resonator area to the busbars of the device. This is identified as LSAWs and Rayleigh waves being radiated to the busbars and transversely excited Rayleigh waves.

The radiation of LSAWs to the busbars strongly depends on frequency, and it may result in significant losses. Although the resonance and the antiresonance depend on the width, height, and shape of the electrodes and the geometry of the structure, the frequency characteristics of the busbar radiation are governed by the relative aluminum thickness in the busbars. For the typically employed electrode thicknesses, the frequency region in which the side radiation is viable occurs inside the stopband and sometimes even includes the resonance frequency.
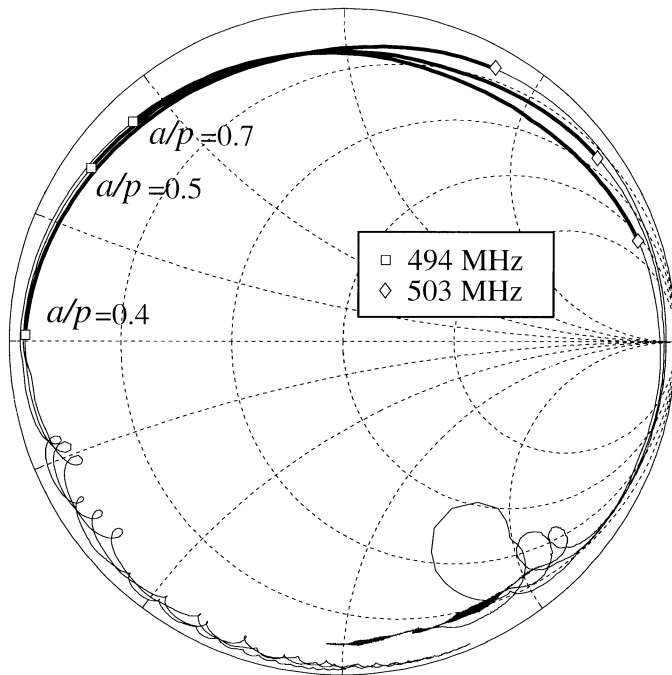
Fig. 11. Measured S_{11} parameter for test structures with varying metallization ratio a/p. Thick curves: the frequency interval prone to busbar radiation with onset at 494 MHz (square) and quenching at 503 MHz (diamond). For $a/p = 0.4$, the onset coincides with the resonance; for higher values, it occurs in the stopband.

A phenomenological simulation was constructed to estimate the losses caused by the LSAW busbar radiation, the excitation of the fs-BAWs, and LSAW attenuation caused by coupling to ss-BAWs. According to the simulations, the busbar radiation well explains the experimentally observed increase in the conductance close to the resonance frequency. Experiments confirm that the magnitude of the radiation depends only weakly on the aperture. Consequently, relative losses are pronounced for narrow apertures.

At high frequencies, above the stopband, the radiation of fs-BAWs is the dominant loss mechanism. However, none of the phenomena studied explains the large magnitude of the losses observed experimentally close to the antiresonance. The residual excitation of slow shear bulk waves and the acoustic attenuation in the aluminum electrodes are among the remaining loss mechanisms that require investigation. Comprehensive experiments or a rigorous theoretical simulation may be required to find the means to minimize the losses and, thus, to optimize the resonator performance.

ACKNOWLEDGMENTS

REFERENCES

[1] K. Hashimoto, M. Yamaguchi, S. Mineyoshi, O. Kawachi, M. Ueda, G. Endoh, and O. Ikata, "Optimum leaky-SAW cut of LiTaO$_3$ for minimised insertion loss devices," in *Proc. 1997 IEEE Ultrason. Symp.*, pp. 245–254.

[2] H. H. Ou, N. Inose, and N. Sakamoto, "Improvement of ladder-type SAW filter characteristics by reduction of inter-stage mismatching loss," in *Proc. 1998 IEEE Ultrason. Symp.*, pp. 97–102.

[3] V. P. Plessky, D. P. Chen, and C. S. Hartmann, "'Patch' improvements to COM model for leaky waves," in *Proc. 1994 IEEE Ultrason. Symp.*, pp. 297–300.

[4] J. V. Knuuttila, P. T. Tikka, C. S. Hartmann, V. P. Plessky, and M. M. Salomaa, "Anomalous asymmetric acoustic radiation in low-loss SAW filters," *Electron. Lett.*, vol. 35, pp. 1115–1116, 1999.

[5] J. V. Knuuttila, P. T. Tikka, and M. M. Salomaa, "Scanning Michelson interferometer for imaging surface acoustic wave fields," *Opt. Lett.*, vol. 25, pp. 613–615, 2000.

[6] J. Koskela, J. V. Knuuttila, P. T. Tikka, M. M. Salomaa, C. S. Hartmann, and V. P. Plessky, "Acoustic leakage mechanism for leaky SAW resonators on lithium tantalate," *Appl. Phys. Lett.*, vol. 75, pp. 2683–2685, 1999.

[7] J. V. Knuuttila, J. Koskela, P. T. Tikka, M. M. Salomaa, C. S. Hartmann, and V. P. Plessky, "Asymmetric acoustic radiation in leaky SAW resonators on lithium tantalate," in *Proc. 1999 IEEE Ultrason. Symp.*, pp. 83–86.

[8] J. Koskela, V. P. Plessky, and M. M. Salomaa, "Theory for shear horizontal surface acoustic waves in finite synchronous resonators," *IEEE Trans. Ultrason., Ferroelect., Freq. Contr.*, vol. 47, pp. 1550–1560, Nov. 2000.

[9] S. V. Biryukov, Y. V. Gulyaev, V. V. Krylov, and V. P. Plessky, *Surface Acoustic Waves in Inhomogeneous Media*. Springer-Verlag, 1995, pp. 255–259.

[10] G. Kovacs, M. Anhorn, H. E. Engan, G. Visintini, and C. C. W. Ruppel, "Improved material constants for LiNbO$_3$ and LiTaO$_3$," in *Proc. 1990 IEEE Ultrason. Symp.*, pp. 435–438.

[11] S. V. Biryukov and M. Weihnacht, "The effective permittivity in the complex plane and a simple estimation method for leaky wave slowness," in *Proc. 1996 IEEE Ultrason. Symp.*, pp. 221–224.

[12] C. S. Hartmann, B. P. Abbott, S. Jen, and D. P. Chen, "Distortion of transverse mode symmetry in SAW transversely coupled resonators due to natural SPUDT effects," in *Proc. 1994 IEEE Ultrason. Symp.*, pp. 71–74.

[13] H. A. Haus and K. L. Wang, "Modes of a grating waveguide," *J. Appl. Phys.*, vol. 49, pp. 1061–1069, 1978.

[14] C. S. Hartmann, V. P. Plessky, and S. Jen, "112°-LiTaO$_3$ periodic waveguides," in *Proc. 1995 IEEE Ultrason. Symp.*, pp. 63–66.

[15] S. Rooth and A. Rønnekleiv, "SAW propagation and reflections in transducers behaving as waveguides in sense of supporting bound and leaky mode," in *Proc. 1996 IEEE Ultrason. Symp.*, pp. 201–206.

[16] M. Solal, J. V. Knuuttila, and M. M. Salomaa, "Modelling and visualization of diffraction like coupling in SAW transversely coupled resonator filters," in *Proc. 1999 IEEE Ultrason. Symp.*, pp. 101–106.

[17] Y. Zhang, J. Desbois, and L. Boyer, "Characteristic parameters of surface acoustic waves in periodic metal grating on a piezoelectric substrate," *IEEE Trans. Ultrason., Ferroelect., Freq. Contr.*, vol. 40, pp. 183–192, May 1993.

Julius Koskela received the MSc, LicTech, and DrTech degrees in technical physics at the Helsinki University of Technology (HUT) in 1996, 1998, and 2001, respectively. His research interests include SAW physics and modeling SAW devices. After his doctoral dissertation, he joined the Nokia Group; he is currently working at the Nokia Research Center. He is a member of the Finnish Physical Society.

Jouni V. Knuuttila received the MSc degree in technical physics at the Helsinki University of Technology (HUT) in 1998. He is a postgraduate student in the Materials Physics Laboratory at HUT. His research interests include optical imaging of surface and bulk acoustic waves, sonoluminescence, and audio signal processing. He is a member of the Finnish Optical Society.

Tapani Makkonen (M'98) received the MSc degree in technical physics at the Helsinki University of Technology in June 1996, after which he continued to work in the Materials Physics Laboratory as a DrTech student. His research interests include the modeling of package parasitic effects in SAW devices; currently, he is focusing on the FEM of crystal resonators. Makkonen is a member of the Finnish Physical Society.

Victor P. Plessky (M'93) received his PhD degree in physical and mathematical sciences at the Moscow Physical-Technical Institute and the DrSc degree at the Institute of Radio Engineering and Electronics (IRE, Russian Academy of Sciences, Moscow) in 1978 and 1987, respectively. Beginning in 1978, he worked at IRE, first as a junior researcher and, in 1987, was promoted to the position of Laboratory Director. In 1991, he also worked as a part-time professor at the Patris Lumumba University, Moscow. He received the full professor title in 1995 from the Russian Government. In 1992, he joined ASCOM Microsystems SA in Bevaix, Switzerland, where he worked as a special SAW projects manager. He was a visiting professor at the Helsinki University of Technology in April and May 1997 and again in spring 2001. Since 1998, he has been working at Thomson Microsonics (presently Thales Microsonics). He has been engaged in research on semiconductor physics, SAW physics (new types of waves, scattering and reflection on surface irregularities, laser generation of SAW), SAW device development (filters, delay lines, RACs), and magnetostatic wave studies. Currently, his interests focus on SAW physics and low-loss SAW filter development. Prof. Plessky is an IEEE member. He was awarded the USSR National Award for Young Scientists in 1984.

Martti M. Salomaa (M'94) received his DrTech degree in technical physics from Helsinki University of Technology (HUT) in 1979. Thereafter, he worked at UCLA and the University of Virginia. From 1982 to 1991, he was the theory group leader at the Low Temperature Laboratory, HUT, and from 1988 to 1991, he served as the director of the ROTA project between the Academy of Finland and the Soviet Academy of Sciences. He has held a sabbatical stipend at the University of Karlsruhe, and, in 1994, he was a guest professor at ETH-Zürich. Since 1996, he has been a professor of technical physics and the Director of the Materials Physics Laboratory in the Department of Technical Physics and Mathematics at HUT. He is a co-recipient of the 1987 Award for the Advancement of European Science (presented by the Körber Foundation, Hamburg). His research interests include BEC, superfluidity, superconductivity, magnetism, physics of SAW, nondiffracting waves, nanoelectronics, mesoscopic physics, and sonoluminescence. He is a member of the IEEE, APS, EPS, and the Finnish Physical and Optical Societies.